Journal of Marine Research, 56, 995–1027, 1998

Generalized inverse with shipboard current measurements: Tidal and nontidal flows in Long Island Sound

by Philip S. Bogden[1,2] and James O'Donnell[2]

ABSTRACT

A simple linear shallow-water model forced by tidal boundary conditions can capture most of the tide height variability in Long Island Sound. In this sense, the tides are easy to model. The modeled tidal currents can be subtracted from measurements in order to obtain estimates of subtidal circulation. But linear shallow-water dynamics is not accurate enough for this purpose. Allowing for dynamical errors with a generalized inverse model leads to improved estimates of tidal and nontidal flow. The analysis provides expected errors for the prior (before inversion) and posterior (after inversion) tidal velocity field.

Estimates of the flow field in central Long Island Sound are obtained with current measurements from a ship-mounted Acoustic Doppler Current Profiler (ADCP) survey. Inversion of data from a single ten-hour survey improves tidal predictions, as verified with independent data. Furthermore, the posterior penalty functional is shown to be an effective test statistic for the existence of nontidal flow. The inverse model reduces model-data misfit, using interior dynamics and open-boundary conditions as weak constraints. Model-data misfit can also be reduced by tuning the friction parameter in the prior tidal model. However, in contrast with inversion, tuning degrades predictability.

1. Introduction

Remarkable technological advances in acoustic Doppler current profiles (ADCP's) have made the measurement of currents from aboard moving ships a routine procedure. In coastal waters, where both precise navigation and bottom tracking are possible, absolute velocity measurements have a precision of several cm/sec or less. Nevertheless, an outstanding limitation of ship-mounted ADCP measurements arises during interpretation of the data. Whereas a single regional survey can provide good spatial resolution of the current field, it may yield little or no resolution of its time variation. The sampling problem is particularly severe in coastal waters with strong tides because tidal and nontidal flows can become indistinguishable.

The objective here is to estimate the evolving field of depth-averaged tidal currents from a regional ADCP survey. The tides are then removed from the data to reveal the nontidal flow. There is little observational evidence for residual currents in the study region, so tidal

1. Department of Geology and Geophysics, Yale University, New Haven, Connecticut, 06520-8109, U.S.A.
2. Present address: Department of Marine Sciences, University of Connecticut, Avery Point, Groton, Connecticut, 06340, U.S.A.

flow speeds are expected to be several times larger than nontidal flows. Tide removal (i.e., "detiding" the data) involves the difference of two nearly equal numbers, so an accurate tidal estimate is critical. The analysis described here exploits a simple model of tidal dynamics to estimate the tidal currents. Allowance is made for errors in both the model and the data.

Tidal models of varying complexity are used in the analysis of ADCP data. The simplest model is periodicity at known frequencies. Standard harmonic analysis yields tidal amplitude and phase, and nontidal flow can be obtained by subtracting the tidal component from the data. Accurate estimates require a well-resolved time series. Many investigators have tried to overcome the poor time resolution of ship surveys by repeating a single ship track, thereby generating a set of time series at several locations along the track. Simpson *et al.* (1990) used this approach to identify tidal and nontidal currents as a function of depth along a single repeated transect line, and Geyer and Signell (1990) repeated several trapezoidal ship tracks to obtain horizontal maps of tidal and residual flow. The accuracy of these techniques is heavily dependent on having a large number of repeated surveys.

Candela *et al.* (1990, 1992) developed a more sophisticated least-squares method for estimating spatially variable tidal amplitude and phase. This can provide useful information from a single regional survey, which allows the ship to sample a larger area. However, the technique uses an arbitrary set of functions to interpolate data in space. Smooth solutions are ensured by restricting the number of functions in the fit, but the fitted functions have no physical justification. Münchow *et al.* (1992) compared several methods of "detiding" ADCP records and concluded that some combination of repetitive ship tracks and least-squares methods provided the best estimates of residual current.

An alternative approach is to simulate the tides with a dynamical model and subtract model predictions from the data. But errors in the tidal model can become indistinguishable from sampling errors in the data. Foreman and Freeland (1991) used a numerical simulation along with the least-squares method of Candela *et al.* (1990). They concluded that the best estimates were obtained by combining elements of both techniques.

This paper describes a generalized inverse method for estimating the barotropic tide from a ship survey. The inverse analysis has distinct advantages over the methods described above because it incorporates dynamics into the statistical framework of minimum-variance estimation. (Egbert and Bennett (1996), discuss the relation with Gauss-Markov estimation.) The inverse looks superficially like a least-squares function fit in that the effects of inversion can be written as a finite sum of functions that vary in space and time. But the resemblance is only superficial because the choice of basis functions is not *ad hoc.* Basis functions for the generalized inverse, referred to as "representers" (see Bennett, 1992), are determined with the dynamical model and its expected error statistics. Inversion provides improved tidal currents, and their expected error statistics, for the entire survey region. Bennett (1992) provides a thorough and enlightening presentation of the generalized inverse theory, along with a variety of oceanographic applications.

Dowd and Thompson (1996) performed an inverse analysis of ship-mounted ADCP data

with similar objectives. They adjusted open-ocean boundary conditions of their model to obtain improved estimates of tides. The interior dynamics remained unchanged in their solution. This proved adequate for their regional model of the continental shelf, where bathymetry variations are much smaller than those in Long Island Sound. In the analysis here, dynamical errors are expected to be relatively large within the inverse model domain, so the interior dynamics is adjusted along with the open boundary conditions.

The generalized inverse provides a formalism for hypothesis testing. Our research (alternative) hypothesis is that there is low-frequency nontidal flow. We support the research hypothesis by falsifying its converse, the null hypothesis. Under the null hypothesis, data are a combination of tidal flow and errors, and the tidal model has errors as well. The null hypothesis includes specification of the error statistics. Two outcomes are possible from the analysis. In one case, a statistically consistent match of data and dynamics leads to acceptance of the null hypothesis. The alternate outcome obtains when no statistically consistent match can be found. If this occurs, the null hypothesis must be re-evaluated. This can be the more interesting scientific outcome because one learns something from the data, namely, that the prior assumptions are wrong. This is also the outcome that can provide support for the hypothesized nontidal flow.

Section 2 of this paper shows that a linear barotropic tidal model can accurately reproduce more than 90% of the mean-square variation in ADCP data from central Long Island Sound. Despite this high model skill, the remaining 10% contains obvious tidal variation. Section 3 describes the null hypothesis for this study, which states that model-data misfit arises from a combination of correlated error from the tidal model and uncorrelated error from sampling. Under this hypothesis, there is no large-scale nontidal flow. Results in Section 4 show that statistically consistent results are not always possible using data from a one-day survey. Violation of the null hypothesis generally occurs when the posterior data misfit show evidence of large-scale subtidal flow. A predictability study using independent data is used to test the accuracy of the tidal inverse. These experiments are used to compare the inverse analysis to a simple example of parameter fitting. Results are discussed in Section 5.

2. Model-data comparison: Prior

The first step in the inverse analysis is to develop a tidal model for a region surrounding the observations. This model is referred to as the "prior." It represents the best estimate of the tides that can be obtained without ADCP data. Model bathymetry includes all of Long Island Sound (Fig. 1). The Sound is roughly 200 km long, 25 km wide and 30 meters deep, and lies between Connecticut and Long Island, New York. Most of the freshwater input comes from the Connecticut River, near the opening to the Atlantic. Primary forcing for the tides in the Sound comes from the eastern opening to the North Atlantic, where semidiurnal tidal amplitude is approximately five times diurnal (Moody *et al.,* 1984). In the west, there is relatively little communication at tidal frequencies with the Hudson River estuary through the East River.

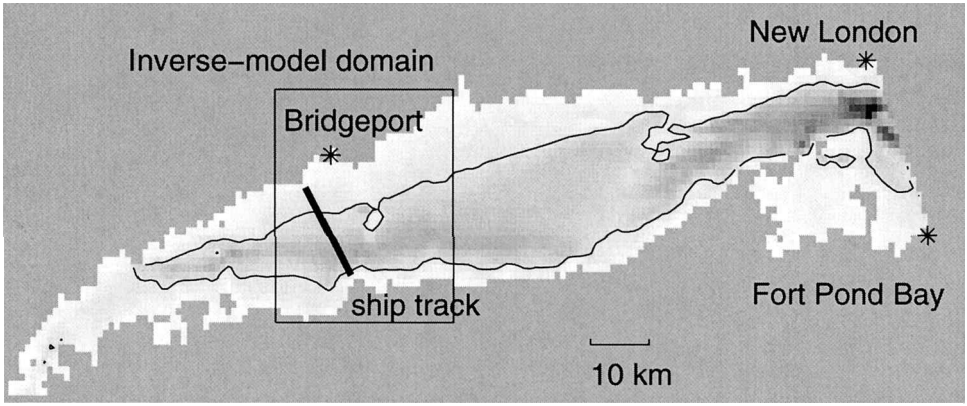

Figure 1. Long Island Sound bathymetry for the prior tidal model. The 20 m isobath is shown by the thin solid line. Darker shading is deeper water. The rectangle outlined in the central Sound is the inverse-model domain. The thick solid line is the ship track that was sampled repeatedly when acquiring data for this study. The closed bathymetry contour just east of the ship track is Stratford Shoal.

a. Data

Current measurements were obtained in central Long Island Sound by repeatedly sampling a single transect (Fig. 1) up to six times daily. This yielded 10 days of data during a two-week period in the summer of 1995. The current observations were obtained using an R. D. Instruments 1200 kHz broadband Acoustic Doppler Current Profiler (ADCP). The instrument was mounted on the keel of the R. V. *Oceanus* (a 26-foot Grady White cabin cruiser, not to be confused with the UNOLS vessel of the same name) with the transducer heads located 0.8 m below the surface. Data were collected using a personal computer that also logged the vessel speed and position from a Magnavox MX200 and 50 R differential global positioning navigation system (GPS). This equipment provided water velocity measurements from 1.75 m to the minimum of 25 m depth and 0.85 times the total depth.

The ADCP compass was calibrated using the method of Joyce (1989). Ship velocity relative to the bottom can be obtained by differentiating the GPS positions and by combining the ADCP's bottom return with the compass heading. Comparison of the two velocity estimates allows determination of any compass bias. Corrections of −2.5 degrees and 0.6 degrees were applied to data collected on northbound and southbound headings, respectively.

Data of questionable reliability were discarded. These include (1) data obtained during CTD casts, (2) data values with "percent good" indicator (R. D. Instruments, 1995) of less than 100 and (3) entire profiles for which less than half the bins were acceptable by the first two criteria. Depth-averaged velocity was computed by (1) averaging the available data, and (2) integrating over depth with linear interpolation between data bins and extrapolation to the surface and bottom with zero shear. These two calculations disagree when the data

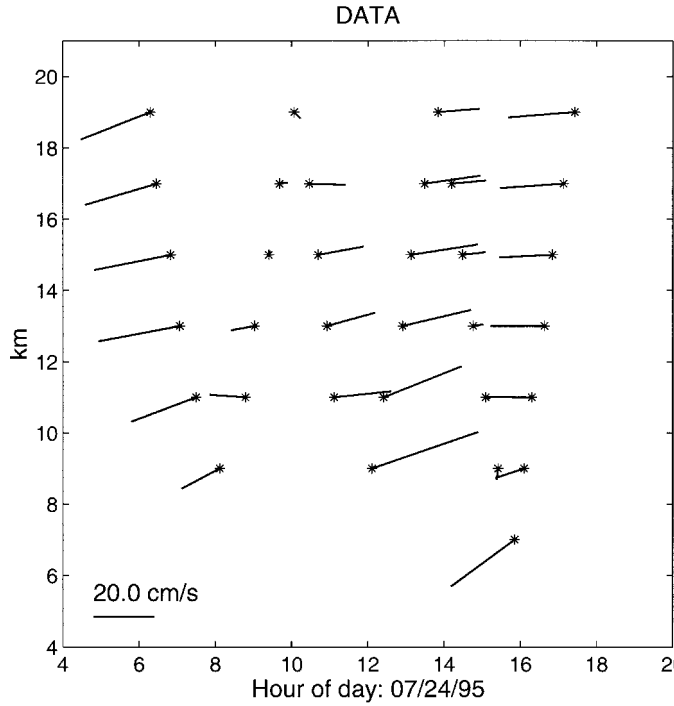

Figure 2. Binned and depth-averaged ADCP data for July 24, 1995. The horizontal coordinate is time, the vertical coordinate is north-south position. The vectors, with asterisks at their bases, represent flow velocity using the scaling in the lower left. For the vectors, left is west and the top of the page is north. On this day, maximum flood occurs at 6:00 in the morning, with ebb 6 hours later.

have large vertical shear near the extremities of the profile. When disagreement exceeded 1.5 cm/sec, the profile was discarded. Depth-averaged velocities were bin-averaged onto the 1 km model grid. Although winnowing eliminates approximately 80% of the data, the remaining profiles still over-resolve the data bins. Figure 2 shows results for a typical one-day survey. Westward tidal currents near 30 cm/s occur during flood, with eastward currents six hours later during ebb.

b. Data error

Errors in the estimation of the depth-averaged velocity, hereafter referred to as data errors, are difficult to evaluate. There is an uncertainty associated with the fact that the ADCP measures at most 85 percent of the water column and another associated with the accuracy of the ADCP measurement. Further discussion necessitates a brief review of the measurement technique. Additional technical details are given by RD Instruments (1995).

The ADCP measures both the water velocity relative to the ship, $\mathbf{u}_r$, and the velocity of the ship relative to the earth, $\mathbf{u}_s$, by measuring the Doppler shift in sound reflected by particles in the water and the ocean bottom, respectively. The signal processing used to

obtain the velocity estimates is different for $\mathbf{u}_r$ and $\mathbf{u}_s$ so separate water and bottom "pings" are used for each. In this application, estimates of $\mathbf{u}_r$ and $\mathbf{u}_s$ were obtained every 10 seconds from 24 pings: 16 water pings for $\mathbf{u}_r$ were interspersed with 8 bottom pings for $\mathbf{u}_s$. An estimate of the average earth referenced water velocity, $\mathbf{u}_w$, was obtained every 10 seconds by adding $\mathbf{u}_r$ and $\mathbf{u}_s$. Using mode 4 processing with a 1200 kHz instrument (see RD Instruments, 1995), the standard error of $\mathbf{u}_w$ should be 1.2 cm/s, and that of ship velocity, $\mathbf{u}_s$, should be 0.1 cm/s. There is also a bias associated with the measurement of the Doppler shift that results in a bias in the current speeds of approximately 1 cm/s. Some of these errors may reduce upon vertical integration and bin-averaging. An upper bound on the associated data error variance is 2.5 cm^2/s^2.

Additional errors arising from ship motion are much larger. Though the ADCP is equipped with tilt and roll sensors, their performance is sensitive to the angular accelerations common to small vessels and high sea states. RD Instruments therefore recommends that $\mathbf{u}_w$ and $\mathbf{u}_s$ be computed in the ADCP beam coordinate system and then transformed to geographical coordinates using the average heading. Ship motion affects Doppler shift of water pings and bottom pings. Since the pings are not simultaneous, ship motion does not exactly cancel in the sum $\mathbf{u}_w = \mathbf{u}_r + \mathbf{u}_s$. Hence, the error in estimating absolute water velocity with $\mathbf{u}_w$ is increased by an amount that depends on the ship's variation in heading, pitch and roll. This measurement error is likely to depend on ship speed, sea state and heading relative to sea and swell. Therefore, the error is likely to be correlated between measurements.

An upper bound on the error of the current measurements can be obtained empirically since the ship's position was determined using a differential GPS navigation system with an uncertainty of approximately 5 m. $\mathbf{u}_s$ can therefore be compared with the ship velocity obtained by differentiating ship location. The ship velocity based on navigation $\mathbf{u}_n$ was computed for straight ship tracks between 1 and 2 km in length (which is comparable to the bin-averaging interval). Therefore, the uncertainty in the velocity of approximately 3 cm/s is less than 1 percent of the ship speed. After $\mathbf{u}_s$ was adjusted for compass bias, we assessed the performance of the bottom-tracking measurement by computing the mean square difference between $\mathbf{u}_n$ and the interval-averaged $\mathbf{u}_s$. The resulting mean-square difference was 59 cm^2/s^2. Eliminating the contribution from uncertainty in $\mathbf{u}_n$, we estimate the mean-square error in the water velocity to be 50 cm^2/s^2. This is the largest potential source of data error. It represents an error associated with bin-averaged velocity that is not reduced by vertical integration to obtain depth-averaged flow. As mentioned above, these errors could be correlated in time and space. The inverse analysis below shows that this *a priori* bound on data error variance is implausibly large.

c. Tidal model

The following simple tidal model reproduces approximately 90% of the mean-square variability in the depth-averaged ADCP data. Linear shallow-water dynamics describes the

motion in a single homogeneous layer,

$$\frac{\partial u}{\partial t} - fv = -g\frac{\partial \eta}{\partial x} - \kappa u \tag{1}$$

$$\frac{\partial v}{\partial t} + fu = -g\frac{\partial \eta}{\partial y} - \kappa v \tag{2}$$

$$\frac{\partial \eta}{\partial t} = -\frac{\partial (Hu)}{\partial x} - \frac{\partial (Hv)}{\partial y}, \tag{3}$$

where $\mathbf{u} = (u, v)$ is depth-averaged flow, η is sea-surface displacement from the average depth H ($\mathbf{x}$), $\kappa = r/H$, $r = 1.5 \times 10^{-3}$ m/s is a friction parameter, and f is constant. No normal flow occurs at the coast,

$$\mathbf{u} \cdot \hat{\mathbf{n}} = 0, \tag{4}$$

and an open boundary condition on sea-surface displacement

$$\eta = \eta_{tide}, \tag{5}$$

is applied at the eastern end of the Sound. (The East River in the west is is treated as a coastal boundary.) Tidal forcing, η_{tide}, is obtained by linearly interpolating sea-surface predictions based on the full suite of N.O.A.A. tidal constituents at New London and Fort Pond Bay (see Fig. 1).

The system is integrated on a standard time-staggered C grid (Mesinger and Arakawa, 1976). The Coriolis term is computed with the $1/H$-weighted four-point average from Platzman (1972). Gridded bathymetry on a 250 m grid, from Dr. Rich Signell (personal communication) of the U.S.G.S., is smoothed and subsampled to obtain the values plotted in Figure 1. For the standard grid spacing of approximately 1 km, the time step is 20 seconds. Integrations are allowed two days to spin up from a state of rest, which is sufficient for results to be independent of initial conditions.

The friction parameter, r, is tuned to maximize the model skill at reproducing N.O.A.A. sea-surface predictions at Bridgeport (see Fig. 1), where sea-surface displacements are roughly twice as large as those at the open boundary. That is, r is selected to minimize the mean-square difference between sea surface at the grid point nearest Bridgeport and reconstructed Bridgeport surface predictions from N.O.A.A. tidal constituents. With the optimal value of r, the mean-square error is less than 3%.

d. Prior skill

Model-data comparisons are made by first sampling the model velocity field in the same way that the moving ship sampled the Sound. An example of the prior velocity field during flood tide on July 24 is shown in Figure 3. Note that the vectors in Figure 3 are plotted at half the actual model resolution, for clarity. The "measured" values of the prior on July 24

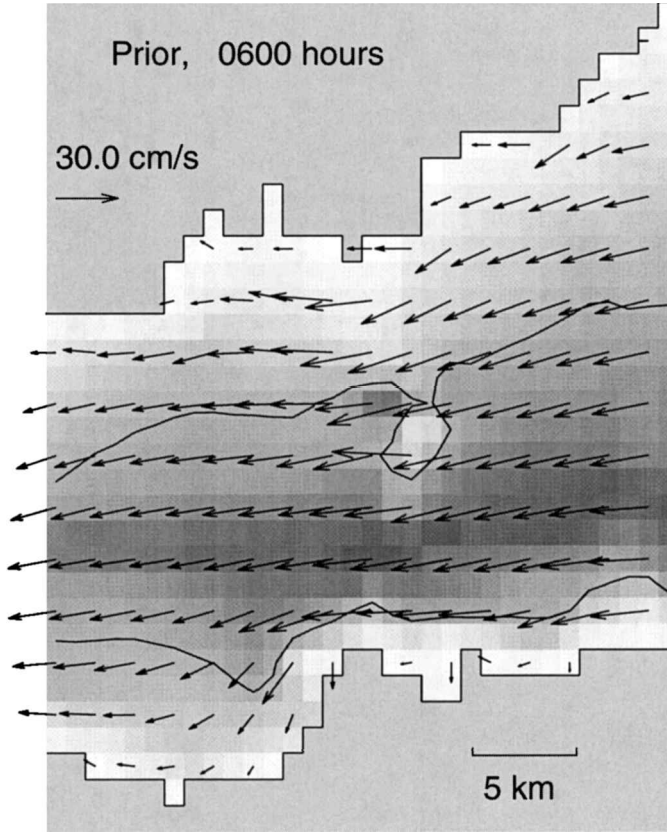

Figure 3. Prior velocity in the inverse-model domain (see Fig. 1). For clarity, velocities are plotted at half the resolution of the model calculation. This field corresponds to flood tide at 6:00 a.m. on July 24. Vectors are superimposed on gray-scale plot of bathymetry along with contours of the 20 m isobath.

appear in Figure 4. The prior misfit (i.e., data minus prior; Fig. 5) has periodic structure indicating that the tidal flow has not been completely removed from the data.

Model "skill" is defined by

$$\text{skill}[\mathbf{u}] = 1 - \frac{(\mathbf{d} - \mathbf{L}[\mathbf{u}]) \cdot (\mathbf{d} - \mathbf{L}[\mathbf{u}])}{\mathbf{d} \cdot \mathbf{d}}, \tag{6}$$

where $\mathbf{d}$ represents a vector of depth-averaged ADCP data and $\mathbf{L}[\mathbf{u}]$ represents a corresponding vector of model "measurements," as in Figure 4. The model is measured with a weighted average of gridded velocity. The weighting function is centered on the location of the corresponding datum and has decay scales of 15-minutes and one kilometer. This is nearly equivalent to evaluating the model at the grid point nearest the datum.

Skill is a quadratic measure of model-data agreement. A maximum skill of 1.0 obtains

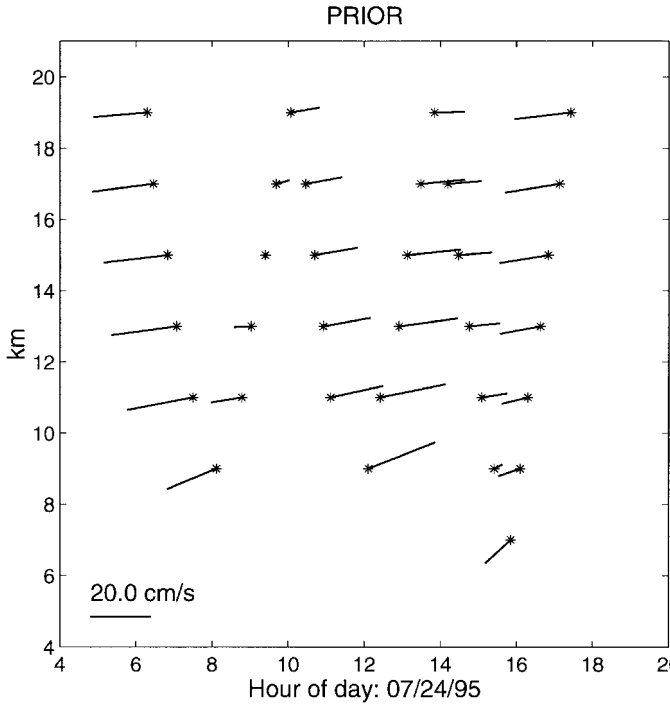

Figure 4. Prior model on July 24. Vectors are obtained by sampling the prior at the locations and times of the data in Figure 2, with identical axis and vector scaling.

with perfect agreement and large negative skills can result when an energetic model has large data misfit. In practice, prior skills range from 0.83 to 0.92. The prior skill of 0.90 for the July 24 data (Fig. 4) is one of the highest.

Data errors make it unreasonable to expect a perfect model to achieve a skill of unity. The data error variance, denoted by Q_d, is the expected mean-square misfit for a perfect tidal model when the data are a combination of tidal velocity and measurement error. For a typical mean-square data variation of 200 cm^2/sec^2, the *a priori* bound of $Q_d = 50$ cm^2/sec^2 discussed above corresponds to a perfect-model skill of 0.75. This is substantially smaller than the prior skills, which indicates that the *a priori* estimate of Q_d is too large.

Q_d is an important parameter in the inverse analysis, and sensitivity to its choice is investigated and discussed below. $Q_d = 16$ cm^2/sec^2 is an *a posteriori* upper bound obtained from the inverse analysis. Unless otherwise stated, it is also the value used in the inverse calculations. With $Q_d = 16$ cm^2/sec^2, the expected skill of a perfect model is 0.92.

3. Dynamical errors and data errors

Despite the ability to account for 90% of the mean-square data variation, structure in the model-data misfit indicates that the prior does not adequately model tidal variability in the

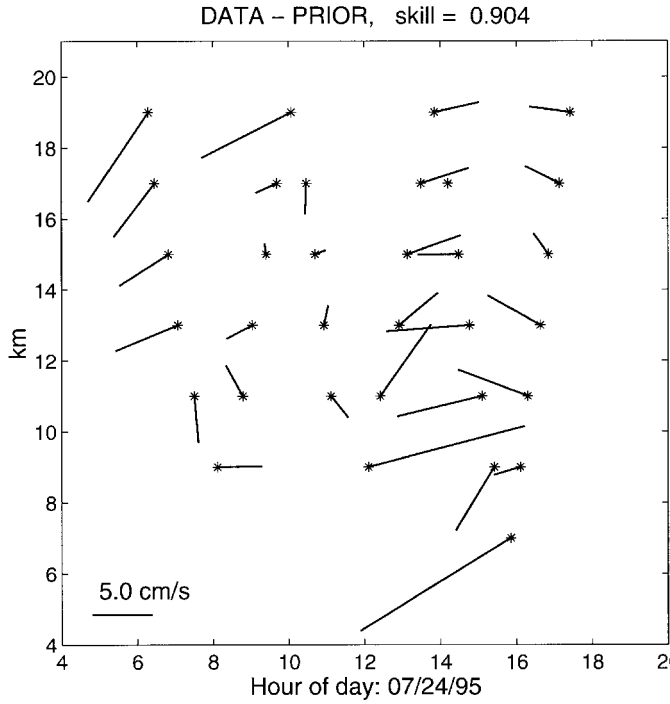

Figure 5. Prior misfit for July 24. Vectors are obtained by subtracting the prior in Figure 4 from the data in Figure 2. Note the four-fold change in vector scaling. Although the prior accounts for over 90% of the mean-square data variation, the prior misfit still exhibits obvious tidal behavior (i.e., 12-hour periodicity).

data. Grid resolution is not the problem since the prior skill does not change with decreased grid spacing. Oversimplified dynamics may be the cause, but it is not clear that a more sophisticated dynamical model would improve skill. In fact, Bogden *et al.* (1996) found that the opposite was true in their analysis of subtidal current measurements in Massachusetts Bay. A hierarchy of models with varying dynamical complexity was examined. The simplest model in the hierarchy had the same dynamics as the tidal model used here. Sequential addition of nonlinearities and depth dependence showed that adding dynamical complexity actually decreased model skill as measured by (6). Of all models tested, the most "realistic" three-dimensional primitive-equation model with sophisticated turbulence closure had the lowest skill at simulating the observed depth-averaged flow. This behavior is reasonable if the more complex nonlinear models have chaotic small-scale flows that are sensitive to model resolution. Measures of model skill other than (6) could be used, and they might lead to different interpretations. Nevertheless, obtaining good model-data agreement with such a sensitive model could require unreasonable effort.

The purpose here is to determine whether plausible errors in the linear tidal model (1) can account for the observed structure in the prior model-data misfit. Dynamical error

statistics, defined below, quantify the notion of "plausible" model adjustment. The inverse method uses ADCP data to improve the tidal model. Our working hypothesis, which may be subsequently rejected, presumes there is no subtidal flow and that all nontidal data variability is uncorrelated error. If this hypothesis is correct, statistically consistent adjustment of the tidal model will eliminate all structure from the model-data misfit.

a. Dynamical errors

The inverse model uses a small portion of central Long Island Sound that is roughly 30 km on a side (the box labeled "Inverse Model Domain" in Fig. 1). In this region, the linear model (1) is modified to allow for errors, so the system becomes

$$\frac{\partial u}{\partial t} - fv = -g\frac{\partial \eta}{\partial x} - \kappa u + \varepsilon_{u_t}, \tag{7}$$

$$\frac{\partial v}{\partial t} + fu = -g\frac{\partial \eta}{\partial y} - \kappa v + \varepsilon_{v_t}, \tag{8}$$

$$\frac{\partial \eta}{\partial t} = -\frac{\partial (Hu)}{\partial x} - \frac{\partial (Hv)}{\partial y} + \varepsilon_{\eta_t}, \tag{9}$$

where, for example, $\varepsilon_{u_t}(\mathbf{x}, t)$ is the unknown error term in the east-west (along-Sound) momentum equation. The coastal boundary condition is unchanged, but the open boundary for the smaller model domain,

$$\mathbf{u} \cdot \mathbf{n} = \sqrt{g/H}\eta + F_{prior} + \varepsilon_{obc}, \tag{10}$$

has a forcing term F_{prior} from the prior and an unknown error term ε_{obc}.

The inverse solution provides "optimal" estimates of the tides and the dynamical errors using an optimality criterion described below. The optimal tidal velocity,

$$\hat{\mathbf{u}} = \mathbf{u}_{prior} + \mathbf{u}', \tag{11}$$

is a linear combination of the prior $\mathbf{u}_{prior}$ and an adjustment $\mathbf{u}'$ that is "driven" by data-based estimates of the dynamical errors. In the absence of ADCP data, $\mathbf{u}' = 0$.

Error statistics are defined with an ensemble average, denoted by angular brackets $\langle\ \rangle$. All dynamical errors are presumed to have zero mean,

$$\langle \varepsilon_{u_t} \rangle = \langle \varepsilon_{v_t} \rangle = \langle \varepsilon_{\eta_t} \rangle = \langle \varepsilon_{obc} \rangle = 0. \tag{12}$$

Consequently, the mean and the prior are identical,

$$\langle \hat{\mathbf{u}} \rangle = \mathbf{u}_{prior}. \tag{13}$$

In concept, individual elements of the ensemble differ because of a variety of factors such as differences in discretized bathymetry, nonlinear effects, stratification effects, friction

parameterization, etc. There is no observational basis for estimating such errors so we choose the simple, yet plausible, statistical model described below.

b. Dynamical error variance

The dynamical error variance constrains the size of adjustments to the prior dynamics. Adjustments will be large where the confidence in (1) is small; i.e., where the dynamical error variance is large. The discussion here focuses on errors from dynamical truncation. Errors arising from discretization are expected to be relatively small because of scaling arguments (e.g., McIntosh and Bennett, 1984) and because model skill does not change with increased grid resolution.

Errors in the momentum equation come from linearization of the dynamics and from an oversimplified drag law. In the x direction,

$$\varepsilon_{u_t}(\mathbf{x}, t) = \varepsilon_{nonlinearity}(\mathbf{x}, t) + \varepsilon_{friction}(\mathbf{x}, t). \tag{14}$$

The errors are presumed to be uncorrelated, $\langle \varepsilon_{nonlinearity}\, \varepsilon_{friction} \rangle = 0$, with variance,

$$\sigma^2_{u_t}(\mathbf{x}) = \langle \varepsilon^2_{u_t} \rangle = \langle \varepsilon^2_{nonlinearity} \rangle + \langle \varepsilon^2_{friction} \rangle. \tag{15}$$

Scale analysis shows that these errors are small relative to the terms kept. Local acceleration $\partial u/\partial t$ scales like $2\pi U/T = 4 \times 10^{-5}$ m/sec^2 for a typical tidal flow speed of $U = 0.3$ m/sec and dominant tidal period of $T = 12.4$ hours. Linearization error scales like $U^2/L \approx 10^{-5}$ m/sec^2, with a horizontal topographic length scale of $L = 10$ km. Errors in the friction parameterization are more difficult to estimate because they depend on stratification, bottom roughness, unresolved turbulence, etc. A 100% error in the friction coefficient κ corresponds to a dynamical error of $\kappa U \approx 10^{-5}$ m/sec^2. Thus, rms dynamical errors are roughly 0.25 times the size of the largest terms in (1). High prior skills provide further evidence that the relative dynamical errors are small.

The prior is used to estimate spatial structure in dynamical error variance. Linearization error variance for the x-direction momentum equation is computed with the time average

$$\langle \varepsilon^2_{nonlinearity} \rangle \equiv \frac{1}{T} \int_0^T (\mathbf{u}_{prior} \cdot \nabla u_{prior})^2 \, dt. \tag{16}$$

Typical values are 10^{-5} m/sec^2, consistent with the scale analysis. The plot of rms error in Figure 6 shows that the largest values occur in regions with large bottom topography gradients.

Errors in the linear drag law are likely to depend on flow speed, so the associated error variance is estimated with a time average of the squared difference between the linear drag law used here and a commonly used quadratic drag law. For the x-direction,

$$\langle \varepsilon^2_{friction} \rangle \equiv \frac{1}{T} \int_0^T \left((C_d |\mathbf{u}_{prior}| - r) \frac{u_{prior}}{H} \right)^2, \tag{17}$$

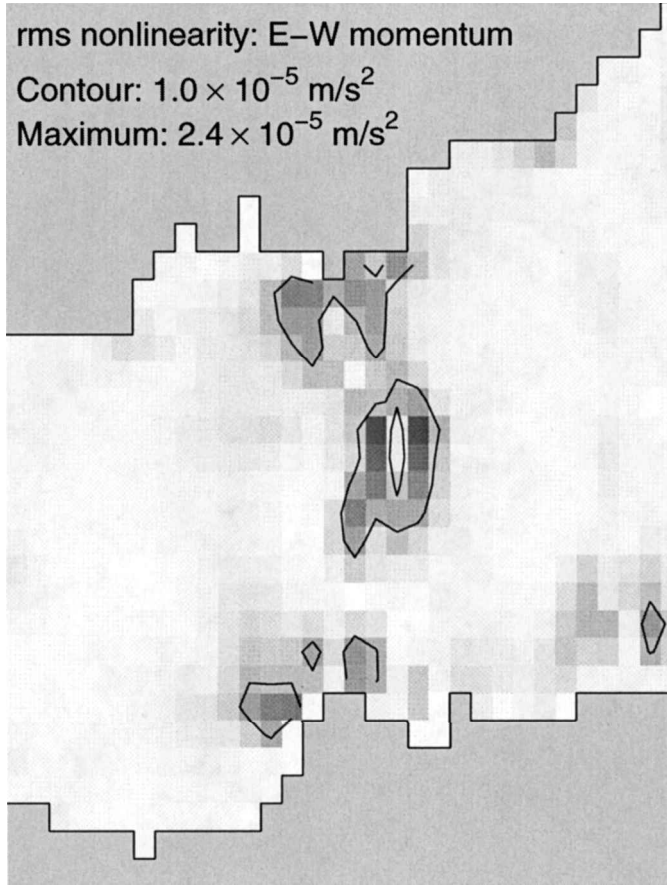

Figure 6. Dynamical error variance from neglected nonlinear accelerations in the along-Sound momentum equation. The 10^{-2} cm/s^2 contour is plotted. The largest values (with darker shading) occur in regions that have strong along-Sound gradients in bathymetry.

where the drag coefficient, $C_d = 0.007$, is selected so that $\kappa \approx C_d|\mathbf{u}|/H$ for typical tidal amplitudes of 30 cm/sec and an average depth of 30 m. These errors have the typical size expected from scaling arguments, with the largest values in shallow water (Fig. 7).

Error variances for the *y*-direction momentum equation (not shown) are computed with v_{prior}. Since tidal currents are oriented along the Sound in the *x*-direction, error variances in the *y*-momentum equation are small relative to those for the *x*-direction.

Linearization error variance $\langle \varepsilon^2_{\eta_t} \rangle$ for the mass conservation equation is computed by time averaging the square of the neglected nonlinear term, $|\nabla \cdot (\mathbf{u}_{prior}\eta_{prior})|^2$. The relative error from linearization scales like that in the momentum equation, and the spatial structure for $\langle \varepsilon^2_{\eta_t} \rangle$ (not shown) is similar to that for $\langle \varepsilon^2_{nonlinearity} \rangle$.

Error variance along the open boundary of the inverse model domain is estimated with the misfit between the prior tide height at Bridgeport and the corresponding N.O.A.A.

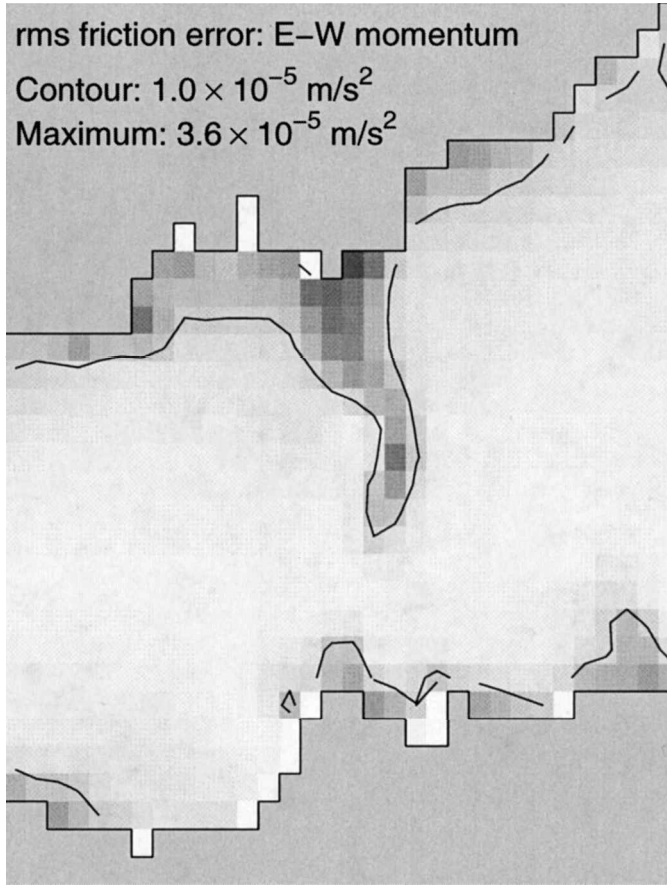

Figure 7. Dynamical error variance from the friction parameterization in the along-Sound momentum equation. (Scaling and contour value are the same as Fig. 6.) The errors here are generally larger than those in Figure 6, especially in the shallow water near the coast and over Stratford Shoal.

prediction. (Recall that the friction coefficient is "tuned" to minimize this quantity.) The rms error, $\sigma_{obc} = 0.12$ m, is roughly 10% of the typical 1 m tidal amplitude at Bridgeport. The corresponding velocity error scales like $\sqrt{g/H}\sigma_{obc} \approx 7$ cm/sec.

c. Error covariance

While dynamical error variances can be estimated with $\mathbf{u}_{prior}$, their correlations are more difficult to determine. The prescription here is simple, plausible and assures that the inverse solution will not change with decreased grid spacing.

Dynamical errors are presumed to be mutually uncorrelated,

$$\langle \varepsilon_{u_t} \varepsilon_{v_t} \rangle = \langle \varepsilon_{u_t} \varepsilon_{\eta_t} \rangle = \langle \varepsilon_{u_t} \varepsilon_{obc} \rangle = \langle \varepsilon_{v_t} \varepsilon_{\eta t} \rangle = \langle \varepsilon_{v_t} \varepsilon_{obc} \rangle = \langle \varepsilon_{\eta t} \varepsilon_{obc} \rangle = 0. \tag{18}$$

Autocorrelations are presumed Gaussian in space and nearly periodic in time. They all have a similar mathematical form. For example, the error covariance for the zonal momentum equation is

$$Q_{u_t} \equiv \langle \varepsilon_{u_t}(\mathbf{x}_1, t_1)\varepsilon_{u_t}(\mathbf{x}_2, t_2)\rangle = G(|\mathbf{x}_1 - \mathbf{x}_2|)F(|t_1 - t_2|)\sigma_{u_t}(\mathbf{x}_1)\sigma_{u_t}(\mathbf{x}_2) \tag{19}$$

where

$$G(|\mathbf{x}_1 - \mathbf{x}_2|) = e^{-(|\mathbf{x}_1-\mathbf{x}_2|^2/D^2)} \tag{20}$$

is the spatial correlation function, and $F(|t_1 - t_2|)$ is the time-lagged correlation function defined below. Note that spatial variation in $\sigma_{u_t}(\mathbf{x})$ introduces inhomogeneity and anisotropy. The decorrelation length scale, $D = 5$ km, is comparable to the smallest resolvable scale in the model (i.e., several times the grid spacing). If D is any smaller, then the numerical grid cannot resolve G and the inverse solution will depend on grid resolution. The covariance effectively filters dynamical errors with spatial scales smaller than D.

Errors in the tidal dynamics are presumed to vary on the same time scales as the tides, i.e., the dynamical error spectrum and tidal spectrum are proportional. Therefore, the time-lagged correlation function F is computed from the prior tidal velocity. Since open-boundary forcing is a sum of multiple tidal constituents, F has roughly a 12.4 hour period. Dynamical errors made during flood will be negatively correlated with errors during the following ebb, and positively correlated with errors during the subsequent flood, roughly 12.4 hours later. Spring-neap modulation accounts for a maximum correlation of 0.85 after one week.

Error in the open boundary condition has covariance,

$$Q_{obc} \equiv \langle \varepsilon_{obc}(s_1, t_1)\varepsilon_{obc}(s_2, t_2)\rangle = G(|s_1 - s_2|)F_{obc}(|t_1 - t_2|)\sigma^2_{obc}, \tag{21}$$

which is similar to (19) except that the two-dimensional position coordinate $\mathbf{x}$ is replaced by distance s along the open boundary.

d. Data error covariance

Data errors include any variability in the depth-averaged flow measurements that differs from the dynamical and statistical definition of tides outlined above. Data error,

$$\boldsymbol{\epsilon}_d = \mathbf{d} - \mathbf{L}[\mathbf{u}], \tag{22}$$

is presumed to be uncorrelated and homogeneous,

$$\langle \boldsymbol{\epsilon}_d \boldsymbol{\epsilon}_d^T \rangle = \mathrm{Q}_d \mathbf{I}, \tag{23}$$

with variance Q_d as described in Section 2. (Sensitivity to the choice of Q_d is discussed in the next section.)

e. The null hypothesis

The definition (23) of the data error covariance does not allow for any low-frequency depth-averaged circulation that might result from tidal rectification, atmospheric forcing, open-boundary forcing, etc. These types of "data error" would exhibit time and space scales that are long relative to the data spacing. Consequently, our working hypothesis is that such large-scale currents do not exist.

The null hypothesis also includes all statistical assumptions about dynamical errors and their prescribed covariances. These error statistics represent a simple and plausible statistical model. Such models are standard in most applications of Gauss-Markov estimation (i.e., objective analysis) such as those discussed by Bretherton *et al.* (1976). For the inverse analysis here, and for minimum-variance estimation in general, the structure of the estimated fields depends upon *a priori* statistics. In standard objective analysis, the statistics are often presumed to be stationary, homogeneous and isotropic so that they can be estimated reliably from the data. These simplifying statistical assumptions are tenuous in coastal regions where bathymetry produces strongly anisotropic and inhomogeneous velocities. It is appropriate, therefore, that bathymetry has a strong influence on the dynamical error covariance described above. Dynamics and bathymetry also help determine the statistics and structure of the estimated velocity field, as described below.

The data are presumed to be a sum of tidal currents and data error. The posterior model-data misfit (i.e., the detided ADCP data) provides an objective measure of nontidal flow. For this reason, the assumption of uncorrelated data error is perhaps the most tenuous element of the null hypothesis. Even though winds were weak during the observation period, there could be important nontidal low-frequency circulation that would violate the null hypothesis. Thus, support for the alternate hypothesis that there is a low-frequency residual circulation is obtained by proving that the converse (the null hypothesis) is false.

f. Minimization criterion

The inverse solution minimizes a weighted sum of squared data errors and dynamical errors. Errors are weighted by their *a priori* covariances. The resulting "penalty functional" takes the form

$$J[\mathbf{u}] = \frac{|\mathbf{d} - \mathbf{L}[\mathbf{u}]|^2}{Q_d} + \int\int\int\int (\varepsilon_{u_t} Q_{u_t}^{-1} \varepsilon_{u_t} + \varepsilon_{v_t} Q_{v_t}^{-1} \varepsilon_{v_t} + \varepsilon_{\eta_t} Q_{\eta_t}^{-1} \varepsilon_{\eta_t}) + \int\int \varepsilon_{obc} Q_{obc}^{-1} \varepsilon_{obc}, \tag{24}$$

where shorthand for the multiple integrals expands to

$$\int\int\int\int \varepsilon Q^{-1} \varepsilon = \int d\mathbf{x}' \int d\mathbf{x} \int dt' \int dt \varepsilon(\mathbf{x}', t') Q^{-1}(\mathbf{x}', t', \mathbf{x}, t) \varepsilon(\mathbf{x}, t), \tag{25}$$

and the inverse of a covariance is defined by

$$\int\int\int\int Q Q^{-1} = \delta(x' - x)\delta(y' - y)\delta(t' - t). \tag{26}$$

The fields $\hat{\mathbf{u}}$, $\hat{\eta}$, $\hat{\varepsilon}_{ut}$, $\hat{\varepsilon}_{vt}$, $\hat{\varepsilon}_{\eta t}$ and $\hat{\varepsilon}_{obc}$ that yield the minimum $J[\hat{\mathbf{u}}]$ of (24) are computed using "representers" (e.g., Bennett, 1992).

Representers provide an extremely efficient way of obtaining the unique solution to the inverse problem. Details are presented in the Appendix. Bennett and McIntosh (1982) introduced the formalism of representers to oceanography and Bennett (1992) provides a thorough pedagogical review of the theory. The reader is referred to his book for methodological details. Egbert and Bennett (1996) discuss a variety of approaches to solving tidal inverse problems, focusing on estimation of harmonic tidal constituents. Bogden *et al.* (1996) discuss some of the practical issues used in the time-domain analysis employed here. In general, the "weak-constraint" inverse is a computationally expensive calculation, and Bennett (1992) describes some aspects of gradient-search algorithms (such as the "adjoint method") that can make computational requirements prohibitive. In contrast, calculation of the inverse solutions presented here took about an hour on a DEC 3000/600 (which was a fast desktop workstation in 1996).

4. Results

a. Inverse solution

The inverse provides a posterior (i.e., data-based) estimate of the tidal component of the data. The prior and posterior are similar because the inverse "adjustments" are small relative to the prior. Nevertheless, adjustments account for about half of the mean square prior misfit, which is large enough to obscure any low-frequency residual circulation. Plots of posterior minus prior for the July 24 data (Fig. 8) show the semi-diurnal variability of the tidal adjustments.

The inverse also produces maps of prior misfit for the entire model domain, thereby extrapolating the data into regions without measurements. Again, the adjustments are small compared to the tides but large enough to mask any nontidal flow that might be present. Figure 9 shows the adjustments (i.e., the posterior minus the prior) during flood tide at 0600 on July 24. The velocity adjustments exhibit uniformly westward flow of several cm/sec, which is consistent with the prior misfit at 0600. Figure 9 shows that the adjustments are associated with flow across the open boundary.

In contrast, the velocity adjustments four hours later have much more spatial variation (Fig. 10), with eastward flow near the southern coast and westward flow along the north. This figure emphasizes the spatial structure associated with adjustment of the interior dynamics. The largest velocity adjustments occur near data locations with large prior misfit and large dynamical error variance.

b. Tidal velocity error variance

The representer method provides a straightforward way to compute expected error variance for prior and posterior estimates of the tidal velocity field (see the Appendix). The variance of $\mathbf{u}_{prior} = (u_{prior}, v_{prior})$ is obtained from direct computation of the reproducing

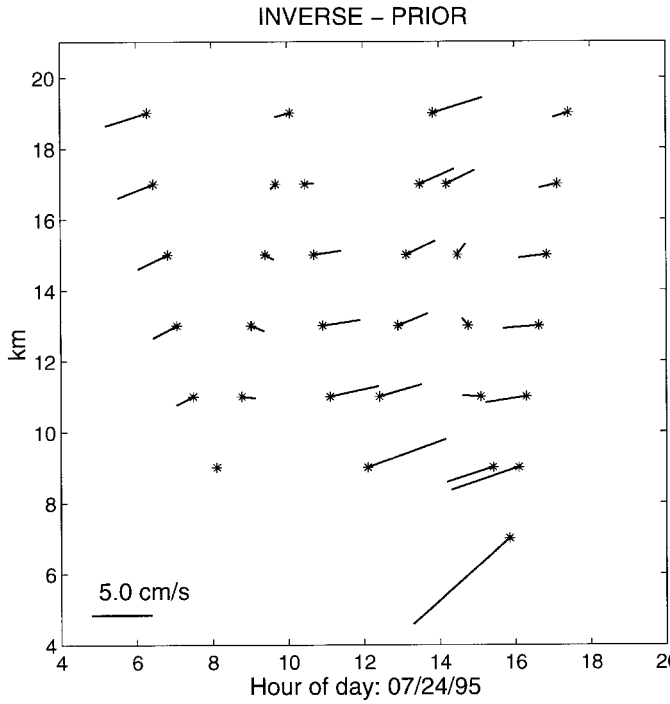

Figure 8. Inverse adjustments to the prior. When these adjustments are added to the prior in Figure 4, one obtains a data-based estimate of the tidal component of the ADCP data. The prior skill is 0.90 and the posterior skill is 0.96. Thus, the inverse adjustments shown here account for over half of the mean-square prior misfit.

kernel (see Bennett, 1992), which "propagates" the dynamical error covariances through the dynamics. This requires calculation of one representer for each grid point, which is time consuming (it took 36 hours on a 1996 vintage workstation). But the prior variance is computed only once because it is independent of the data distribution.

The resulting rms error $\langle (u - u_{prior})^2 \rangle^{1/2}$ for the x-component of tidal flow is highly inhomogeneous (Fig. 11). (This calculation is relatively efficient because, once the prior error variance is known, the necessary elements are computed for the inverse.) Expected errors approach 10 cm/sec in shallow water near the open boundary. In the interior, errors reduce to 4 cm/sec in shallow water and even less in deep water. Velocity errors are nearly isotropic near the open boundaries, while interior errors exhibit the same anisotropy as the tidal currents, which tend to be oriented along isobaths.

Expected errors for posterior tidal velocities depend on the data distribution. Figure 12 shows the rms error $\langle (u - \hat{u})^2 \rangle^{1/2}$ for a hindcast at 0600 on July 24, based on the data from the July 24 survey. The smallest errors, less than 2.0 cm/sec, occur near the ship track and in deep water to the east. Over Stratford Shoal—the shallow region in the center of the

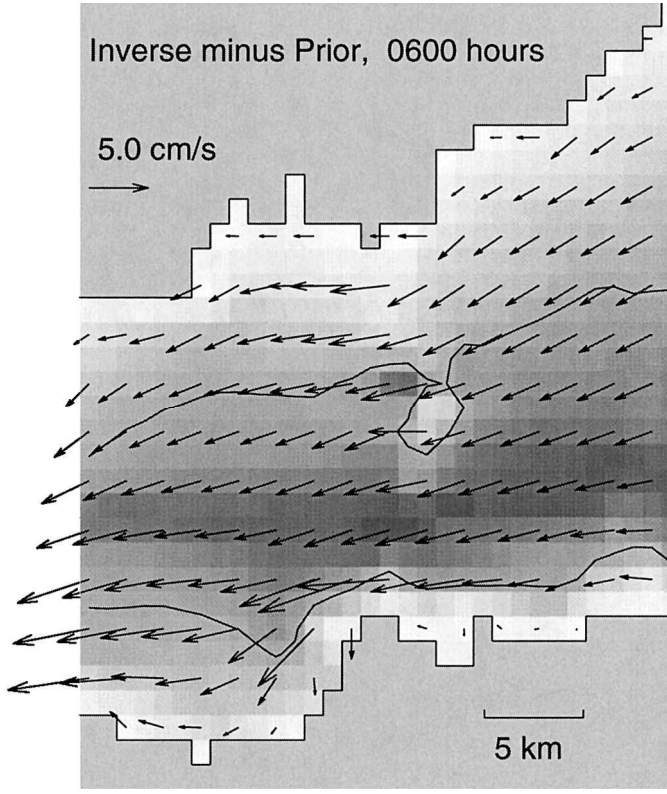

Figure 9. Inverse minus the prior at 6:00 a.m. on July 24. For clarity, every second vector in each direction is plotted. This is the data-based adjustment to the velocity field in Figure 3. Note the change of scale.

inverse model domain—rms error is close to 6 cm/sec, which is not much smaller than the prior error of 8 cm/sec.

Figure 13 shows the fractional reduction in error variance. The largest reduction occurs in the immediate vicinity of the ship track, close to the data. The data influence extends southeast of the ship track in deep water where dynamical errors are small. In this region, tidal improvements are dominated by open boundary condition adjustments. In shallow regions near the boundary and over Stratford Shoal the inverse adjustments have relatively little influence. Improvement in these regions requires direct sampling. Note that this analysis can be used to design effective ship tracks because the posterior error variance depends on the data distribution, not the actual data values.

c. *The hypothesis test*

The prior penalty functional $J[\mathbf{u}_{prior}]$ is a weighted measure of prior misfit,

$$J[\mathbf{u}_{prior}] = (\mathbf{d} - \mathbf{L}[\mathbf{u}_{prior}])^T \mathbf{Q}_d^{-1} (\mathbf{d} - \mathbf{L}[\mathbf{u}_{prior}]), \tag{27}$$

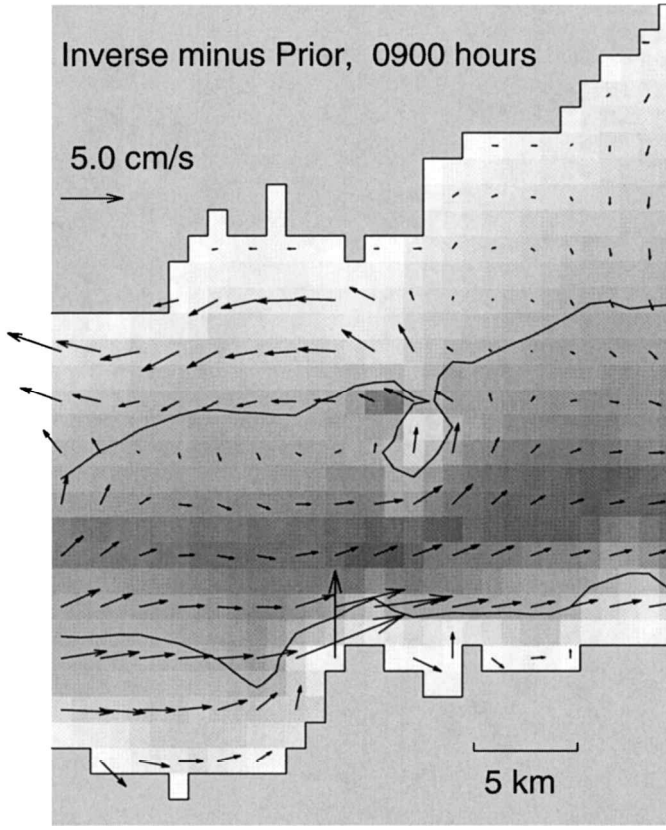

Figure 10. Inverse minus prior at 9:00 a.m. on July 24, 3 hours after the field plotted in Figure 9 (with the same scaling). These adjustments have relatively small horizontal scales.

where $\mathbf{Q}_d = \mathbf{Q}_d\mathbf{I}$ is the data error covariance matrix. This follows immediately from Eq. 24. Table 1 shows $J[\mathbf{u}_{prior}]$ and N for 8 different experiments. In all but one case, $J[\mathbf{u}_{prior}]$ exceeds N as expected. This is reasonable because the prior misfit includes the effects of both dynamical errors and data errors. Since those errors are presumed to be uncorrelated, the expected value of $J[\mathbf{u}_{prior}]$ (which is the sum of the squared prior misfit divided by Q_d) exceeds the number of data values N.

Bennett (1992) shows that the posterior penalty functional $J[\hat{\mathbf{u}}]$ can also be expressed as a weighted measure of prior data misfit,

$$J[\hat{\mathbf{u}}] = (\mathbf{d} - \mathbf{L}[\mathbf{u}_{prior}])^T(\mathbf{R} + \mathbf{Q}_d)^{-1}(\mathbf{d} - \mathbf{L}[\mathbf{u}_{prior}]), \tag{28}$$

where the representer matrix $\mathbf{R}$ is the data covariance due to dynamical error. For suitably distributed data and dynamical errors, $J[\hat{\mathbf{u}}]$ has a Chi-square distribution with N degrees of freedom. So $J[\hat{\mathbf{u}}]$ is a test statistic for the null hypothesis with mean N and standard

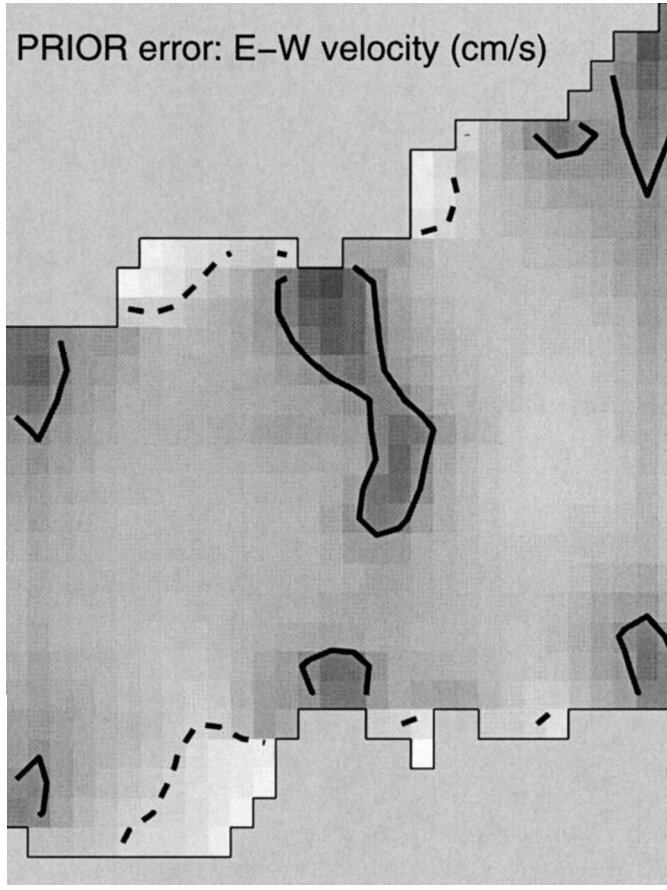

Figure 11. Expected rms error of u_{prior} (**x**, t). The plot shows one standard error of the prior estimate of zonal tidal flow. The 6 cm/sec contour is solid, the 3 cm/sec contour is dashed. These values are obtained by "propagating" the dynamical error covariances through the dynamics. Expected error in the tidal flow is almost everywhere greater than 3 cm/sec, and exceeds 6 cm/sec near the open boundaries and in regions with large dynamical error.

deviation $\sqrt{2N}$. If $J[\hat{\mathbf{u}}]$ departs significantly from the mean, then we reject the null hypothesis.

Results in Table 1 show that $J[\hat{\mathbf{u}}]$ is generally about half of $J[\mathbf{u}_{prior}]$. In four of the eight analyses, $J[\hat{\mathbf{u}}]$ is within one standard deviations of N. Six of the eight lie within two standard deviations of N.

$J[\hat{\mathbf{u}}]$ is 2.7 standard deviations less than the expected value of N for the July 24 analysis. Both $J[\mathbf{u}_{prior}]$ and $J[\hat{\mathbf{u}}]$ are anomalously small for the July 24 data, which would be expected if Q_d were too large. While there is uncertainty in the data error variance Q_d, results below show that a reduction in Q_d of less than 50% would change the conclusions for six of the

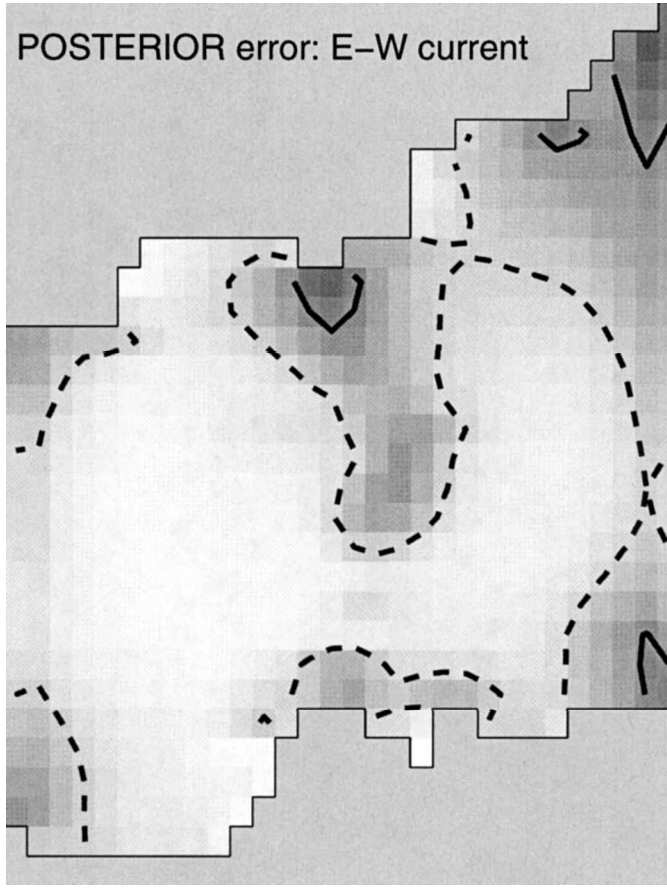

Figure 12. Expected rms error of the posterior tidal velocity $\hat{u}(\mathbf{x}, t)$. This plot shows one standard error of the posterior estimate of zonal tidal flow during the middle of the July 24 survey, based on the July 24 data distribution. The scaling and contours are identical to those in Figure 11.

other seven experiments. It remains unclear why the model performs so well for the July 24 data set.

In contrast, $J[\hat{\mathbf{u}}]$ is 3.0 standard deviations greater than the expected value of N for the July 31 analysis. A time average of the posterior model-data misfit exhibits statistically significant spatial structure, with eastward flow in the south and westward flow in the north (Fig. 15). Large posterior misfits, when they exist, tend to have this orientation. Eastward flows occur for four of the seven days: July 21, 25, 31 and August 02. Westward flows, though less common, occur at the northernmost station on July 25 and 31. These two days have the strongest nontidal residuals and are the only two days for which $J[\hat{\mathbf{u}}]$ exceeds N by more than one standard deviation (Table 1). These analyses provide examples where the null hypothesis is plausibly rejected because of the existence of a residual circulation.

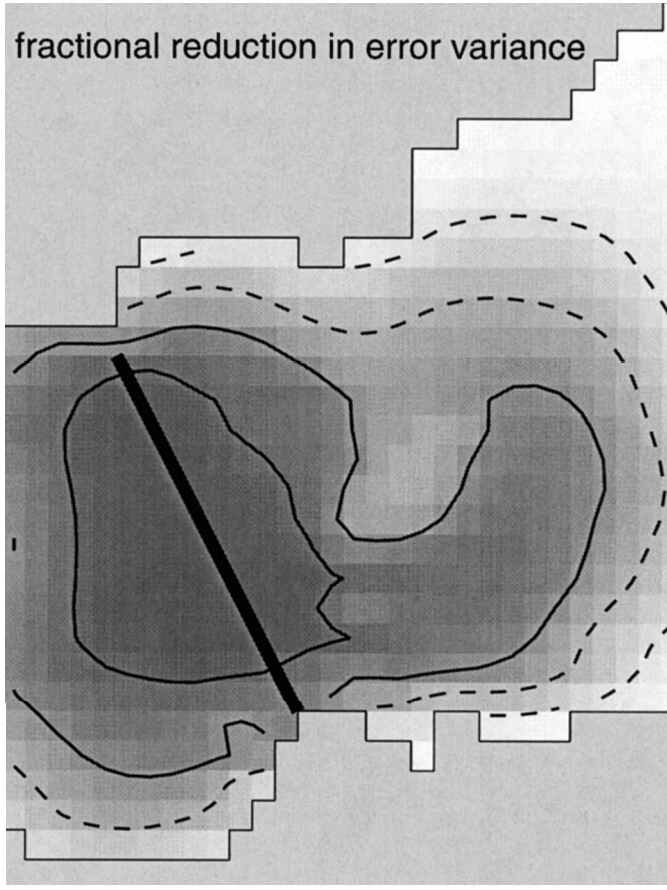

Figure 13. Fractional reduction in expected error variance for the examples in Figures 11 and 12. The 0.2 and 0.4 contours are dashed, the 0.6 and 0.8 contours are solid, and the ship track is superposed on the plot. Large reductions in error variance for zonal tidal flow occur near ship track. Also, the inverse preferentially improves tides in the regions with smooth deep bathymetry. The improvement is relatively poor in shallow regions near the coast and over Stratford Shoal, just east of the ship track.

Furthermore, the results indicate that $J[\hat{\mathbf{u}}]$ provides an objective measure for the existence of low-frequency flow.

In general, inverse adjustments eliminate most of the structure in the prior model-data misfit. This can be seen by comparing the posterior misfit on July 24 (Fig. 14) with the prior misfit in Figure 5. However, even though the model performs anomalously well for this data set, the posterior misfit still exhibits correlation from one location to the next: the final northbound leg between 16:00 and 18:00 shows consistent northward flow, and the previous southward leg shows westward flow for most of the misfit vectors. This evidence

Table 1. Prior and posterior statistics. Results for six one-day inversions and two two-day inversions include prior and posterior values of mean-square model-data misfit, skill and J. The right-most column shows the expected value N for posterior penalty functional $J[\hat{\mathbf{u}}]$ with $\pm$ one standard deviation. For half the analyses, $J[\hat{\mathbf{u}}]$ lies within one standard deviation of N. $J[\hat{\mathbf{u}}]$ is anomalously small for the July 24 analysis, and anomalously large for the July 25 and July 31 analyses. These results were obtained with $Q_d = 16$ cm^2/sec.

	ms misfit (cm/^{2})^2		Skill		J		
Survey	Prior	Posterior	Prior	Posterior	Prior	Posterior	$N \pm \sqrt{2N}$
Jul 20	23.9	10.4	0.861	0.940	41.8	24.5	28 ± 7.5
Jul 21	32.8	16.2	0.832	0.917	110.7	64.7	54 ± 10.4
Jul 24	15.9	6.9	0.904	0.958	65.4	35.1	66 ± 11.5
Jul 25	29.9	18.7	0.876	0.922	115.8	81.7	62 ± 11.1
Jul 31	36.7	21.4	0.872	0.926	123.9	85.3	54 ± 10.4
Aug 2	18.8	12.3	0.919	0.947	79.7	57.6	68 ± 11.7
Jul 20 & 21	29.6	16.1	0.841	0.914	151.8	92.0	82 ± 12.8
Jul 24 & 25	22.7	12.5	0.888	0.938	181.2	112.4	128 ± 16.

of correlated data errors is a violation of the null hypothesis and may account for the anomalously small values of $J[\mathbf{u}_{prior}]$ and $J[\hat{\mathbf{u}}]$ mentioned above.

d. Sensitivity to the choice of Q_d

A tradeoff between model adjustment and posterior data misfit can be controlled with the data error variance parameter Q_d. The relative penalty for model adjustment increases as Q_d increases, and $Q_d \to \infty$ is the worthless-data limit for which the posterior equals the prior. In contrast, $Q_d \to 0$ is the perfect-data limit in which the model interpolates the data, at least in principle. In practice, the inverse becomes ill-conditioned for Q_d substantially less than the values used here, so it is impractical to compute the inverse that interpolates the data.

Posterior skill and posterior misfit are not sensitive to plausible variations in Q_d. This is apparent from Table 2 which shows how the results in Table 1 (averaged over all analyses) vary with Q_d. Although there is uncertainty in the value $Q_d = 16$ cm^2/sec^2 used above, the extreme values of Q_d in Table 2 are unreasonable. The smallest value, 8 cm^2/sec^2, is comparable to measurement precision and the largest value, 32 cm^2/sec^2, exceeds the average prior misfit of 26 cm^2/sec^2 by about 20%. Nevertheless, this 4-fold variation in Q_d makes less than 2% change in mean square posterior misfit and posterior skill. The same insensitivity was observed by Bogden *et al.* (1996) in an analysis of subtidal velocity with mooring data.

In contrast, the posterior penalty functional $J[\hat{\mathbf{u}}]$ is highly sensitive to the same variations in Q_d. Table 2 shows that $J[\hat{\mathbf{u}}]$ varies in almost inverse proportion with Q_d. Recall that $J[\hat{\mathbf{u}}]$ is χ^2 with N degrees of freedom. Since N is large, the standard error $\sqrt{2N}$ of $J[\hat{\mathbf{u}}]$ is much smaller than its mean N. Therefore, the sensitivity to variations in Q_d makes $J[\hat{\mathbf{u}}]$ a useful test statistic.

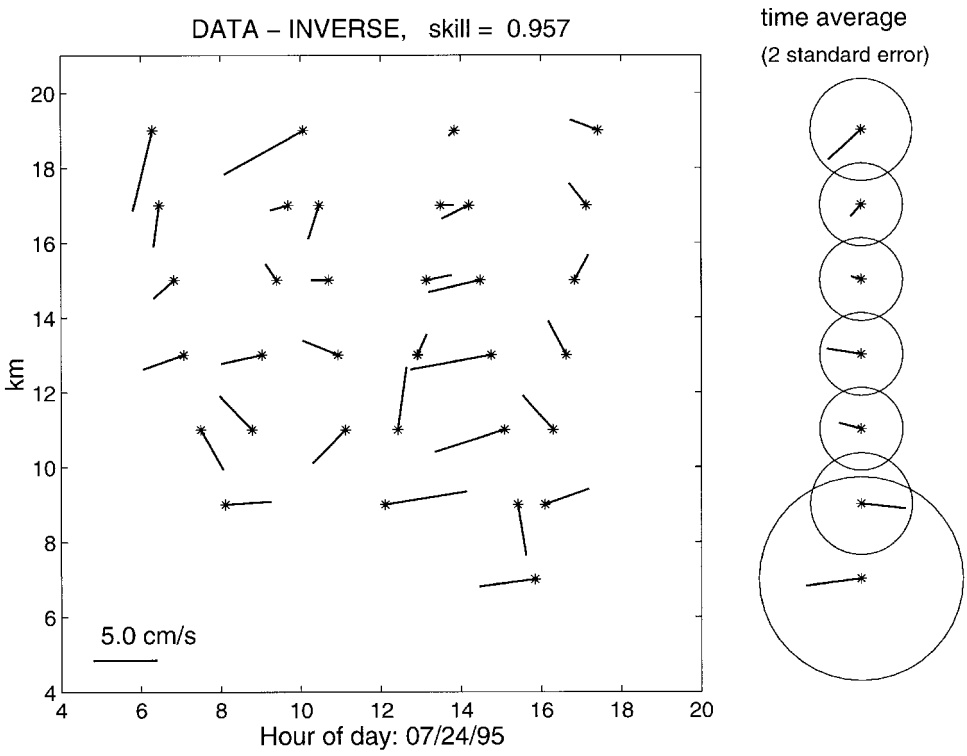

Figure 14. Posterior misfit on July 24. The prior misfit for this analysis is plotted in Figure 5 with the same scaling. The time-averaged vectors are plotted to the right, and the circles have a radius of two standard errors.

e. Predictability

Just as the inverse extrapolates the data into unsampled regions, the inverse also extrapolates in time. The predictive skill of the extrapolated inverse adjustments provides an independent test of the accuracy of the inverse. Under the null hypothesis, dynamical errors are nearly periodic with a maximum correlation of 0.85 after one week. Therefore, a one-day survey should substantially improve the tidal estimates for at least one week into the future.

Predictability is tested using the ten one-day surveys from a 15-day period starting on July 20. Six of the surveys included at least two complete round-trip crossings (4 transects) of the Sound. These provide six realizations for evaluating predictability obtained from a one-day survey. On average, posterior skill exceeds prior skill by 0.06. This is the improvement obtained by hindcasting the data. Predictive improvement for an M-day forecast is the difference between the prior skill on day M and the posterior skill on day M using only the data from day $M = 0$. Results from the six one-day surveys are presented in Table 3 and Figure 16. In general, the inverse improves predictive skill for up to seven days.

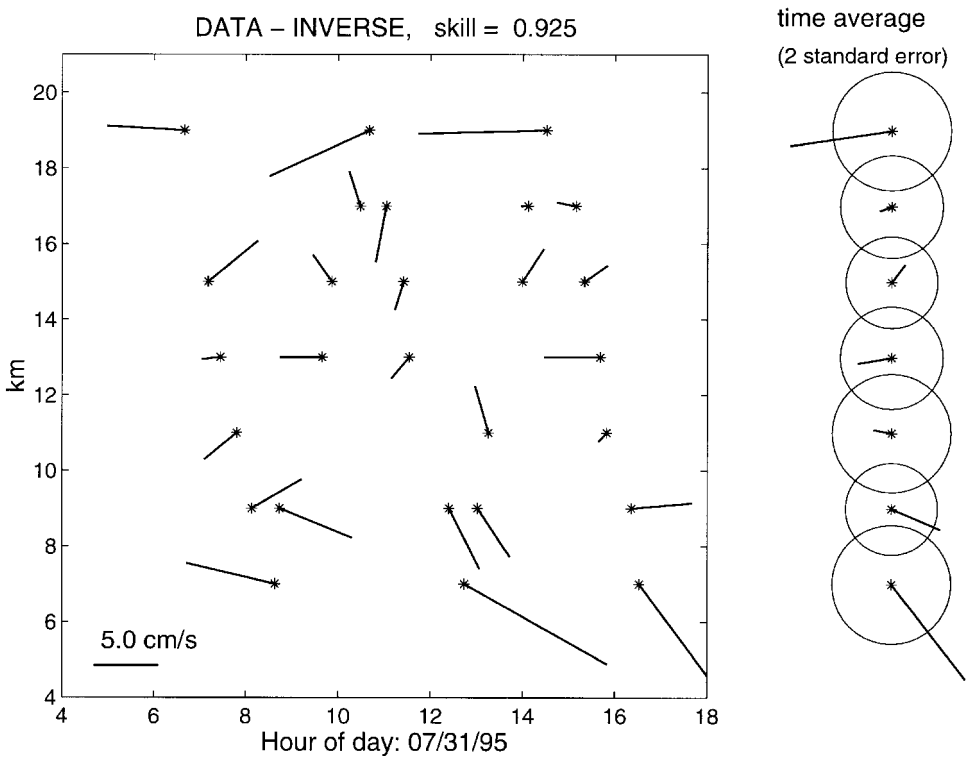

Figure 15. Posterior misfit on July 31. Unlike the misfit in the previous figure, a time average of these values yields statistically significant westward flow in the north and eastward flow in the south. The time-averaged vectors indicate statistically significant eastward flow in the north and westward flow in the south.

However, there is evidence that the increased predictive skill from the inverse has a shorter time scale than expected under the null hypothesis. This is apparent from the interpolated values in Figure 16, and it is evident in all of the individual realizations in Table 3. In each case, the predictive skill drops to zero after about seven days. This is much longer than the semi-diurnal period of the tides, but much shorter than the presumed decorrelation time for dynamical errors. Implications of this result are discussed below.

In principle, longer data sets should provide more independent information and more reliable forecasts. This idea is tested with data with the two cases when complete surveys occurred on two consecutive days. The results are included in Table 3 and Figure 16. As expected, the skill improvement from two-day surveys is generally greater than that from one-day surveys.

f. Is this any better than tuning the friction coefficient?

Under the null hypothesis, the largest dynamical errors come from the friction parameterization. If this is true, then tuning the friction coefficient to the ADCP data might improve

Table 2. Sensitivity to variations in Q_d. This table shows the results of Table 1, averaged over all eight experiments, for a variety of different values of Q_d. Results show that misfit and skill are insensitive to variations in Q_d, while J varies in almost inverse proportion. The value of Q_d marked by an asterisk was used to obtain the results in Table 1, and gives an average $J[\hat{\mathbf{u}}]$ that is close to the average N of 68. While there is some uncertainty in the appropriate choice of Q_d, a value outside the range of 12 to 20 would alter most of the conclusions drawn from Table 1.

			J	
Q_d	Posterior misfit	Posterior skill	Prior	Posterior
32	16.0	0.924	54.4	37.9
28	15.6	0.926	62.2	42.5
24	15.3	0.928	72.5	48.7
20	14.8	0.930	87.1	57.0
16*	14.3	0.936	108.8	69.2
12	13.6	0.936	145.1	88.6
8	12.7	0.941	217.6	125.3

predictive skill for the prior. This is investigated by running the prior for a range of values of r. Table 4 shows the change in prior skill obtained by varying r for each of the one-day surveys. The standard value of 0.0015 m/sec used in the analysis happens to correspond to the optimal value for hindcasting the ADCP data on July 28 and August 2. Based on the ADCP data, the optimal r is smallest for the first two surveys, and becomes progressively larger with time.

It is clear that tuning r to the July 20 survey leads to large negative changes in skill later on. This is generally the case for other surveys. The comparison between tuning and inversion is clearest in Figure 17, which shows the tuning experiments averaged for the same surveys as the one-day inversions in Figure 16. The averaged tuning results are plotted with open circles in Figure 17. For comparison, the asterisks from inversion are identical in Figures 16 and 17. The maximum improvement in hindcast skill obtained by tuning is less than half of that obtained by inversion. For predictions, the increased skill

Table 3. Predictive skill from inversion. Predictive skill = $10^3 \times$ (posterior skill − prior skill). Day 0 corresponds to a hindcast of the data used in the inverse. Predictive skill remains positive for up to a week, sometimes more. These results, averaged over all experiments, are plotted in Figure 16.

	M = days into the future											
Survey date	0	1	2	3	4	5	6	7	8	9	10	11
Jul 20	80	50			19	14			−2			10
Jul 21	84			14	14			22			−11	6
Jul 24	57	31			3			0	−25	10	35	0
Jul 25	47			27			30	−1	14	36	27	
Jul 31	51	23	2	2	23							
Aug 2	30	33	8									
Jul 20 & 21	73			26	25			13			3	
Jul 24 & 25	52			28			27	−10	12	38	24	

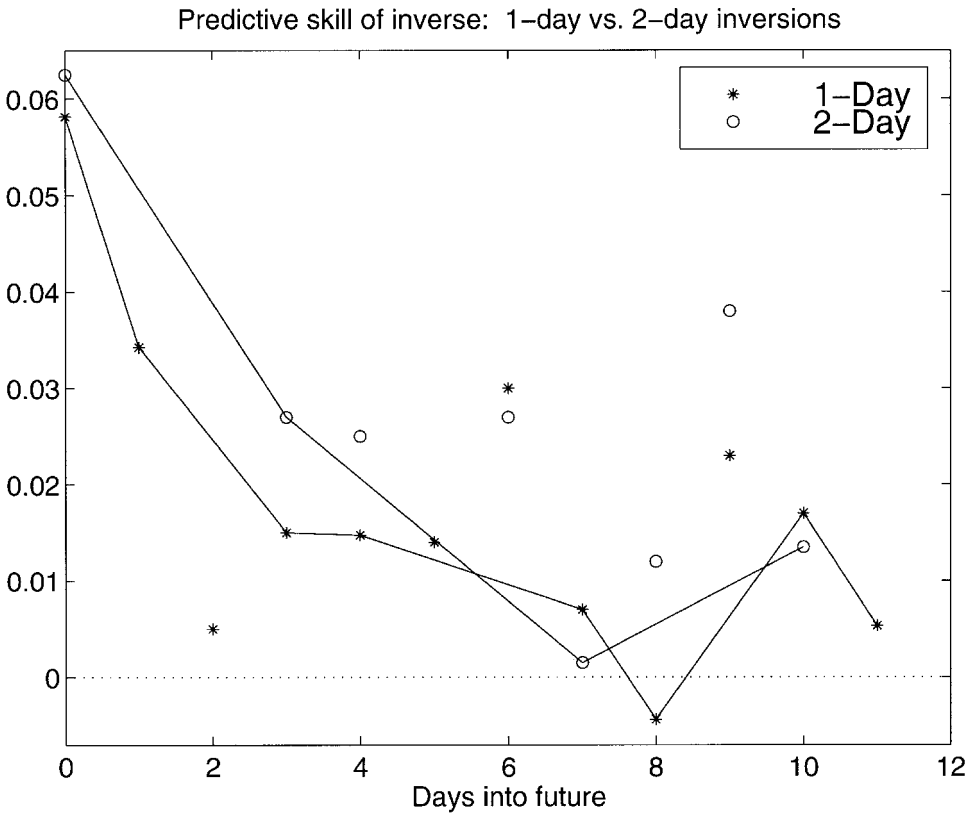

Figure 16. Predictive skill of the inverse. The asterisks mark the change in skill, relative to the prior, due to inversion of the data from one-day surveys. Day zero corresponds to a hindcast, so the day zero value is the difference between posterior and prior skill for the data used in the inverse. Asterisks based on the average of at least three realizations are interpolated. The open circles mark predictive skill for an inverse based upon two surveys made on successive days. Open circles based on at least two such realizations are interpolated.

from inversion approaches zero after a week, whereas the change from tuning becomes decidedly negative. Thus, tuning is worse than inversion, and tuning is worse than nothing because it degrades forecasts.

5. Discussion

Prior skills average 0.87 and posterior skills average 0.94. This means that the inverse adjustments typically account for half of the mean-square misfit between the prior and the data. It also means that, despite such high prior skills, errors in the linear tidal model are comparable in size to nontidal variability in the data. This conclusion is not sensitive to uncertainties in the *a priori* value of data error variance, Q_d.

Table 4. Change in prior skill (×1000) obtained by tuning the friction coefficient, r. The standard value, $r = .0015$ m/sec, is marked by an asterisk in the first column. Results are shown for all days, including those with less than four complete transects. These results show that, for the ADCP data, the standard value is optimal for the July 28 and August 3 surveys.

$r \times 10^3$	Jul 20	21	24	25	28	31	Aug 1	2	3	4
1	54	49	−03	−08	−101	−56	−6	−59	−80	−99
1.1	59	51	17	09	−61	−22	3	−25	−45	−52
1.2	53	46	24	16	−32	−2	9	−5	−21	−22
1.3	39	35	22	16	−14	7	10	4	−7	−6
1.4	21	19	13	10	−4	7	7	5	−1	1
1.5*	0	0	0	0	0	0	0	0	0	0
1.6	−22	−21	−17	−13	−2	−11	−9	−9	−4	−7
1.7	−45	−44	−36	−28	−8	−25	−21	−21	−11	−17

Under the null hypothesis, the measurement error variance Q_d equals the mean-square posterior misfit. *A priori* considerations in Section 2 place an upper bound on Q_d of at least 50 cm^2/sec^2. The average prior misfit is 26 cm^2/sec^2 and never exceeds 37 cm^2/sec^2. This is the first indication that Q_d is less than 50 cm^2/sec^2. The inverse analysis provides an even stronger bound on Q_d. Although the inverse depends on Q_d, a 4-fold variation in Q_d has a small effect on posterior misfit, which ranges from 12.7 to 16.0 cm^2/sec^2. Thus, the inverse provides an *a posteriori* upper bound on measurement error variance (16.0 cm^2/sec^2) that is not sensitive to *a priori* assumptions about Q_d.

The posterior penalty functional $J[\hat{\mathbf{u}}]$ is relatively sensitive to variations in Q_d. This sensitivity makes $J[\hat{\mathbf{u}}]$ a useful test statistic. When $Q_d = 16$ cm^2/sec^2, $J[\hat{\mathbf{u}}]$ lies within one standard deviation of its mean for half of the analyses. For these analyses, there is insufficient evidence to reject the null hypothesis that all nontidal variability in the data is measurement error. When $J[\hat{\mathbf{u}}]$ exceeds N by more than one standard error, a consistent pattern emerges from the posterior model-data misfit. For these analyses, the time averaged misfit exhibits statistically significant westward flow in the north and eastward flow in the south. This shows that $J[\hat{\mathbf{u}}]$ can be used to test for the existence of large-scale subtidal flow.

In retrospect, two modifications of the null hypothesis require further consideration. First, predictability studies indicate that dynamical errors in the prior may decorrelate more quickly than presumed. That is, the time-lagged dynamical error correlation function F may decay to zero after about a week. Second, patterns in the posterior misfit which vary from one ship track to the next indicate the presence of correlated data errors. These patterns are not indicative of subtidal flow because, when $J[\hat{\mathbf{u}}] \geq N$, they can be eliminated by time averaging. If correlated posterior misfit stems from errors in the tidal model, then the dynamical error statistics need modification. If correlated misfit represents correlated measurement error, then the data error covariance needs modification. Ship motion during data acquisition is a likely source of correlated measurement error. Whatever the cause, data error correlation reduces the information content (degrees of freedom) of the data and can impair the accuracy of statistical tests.

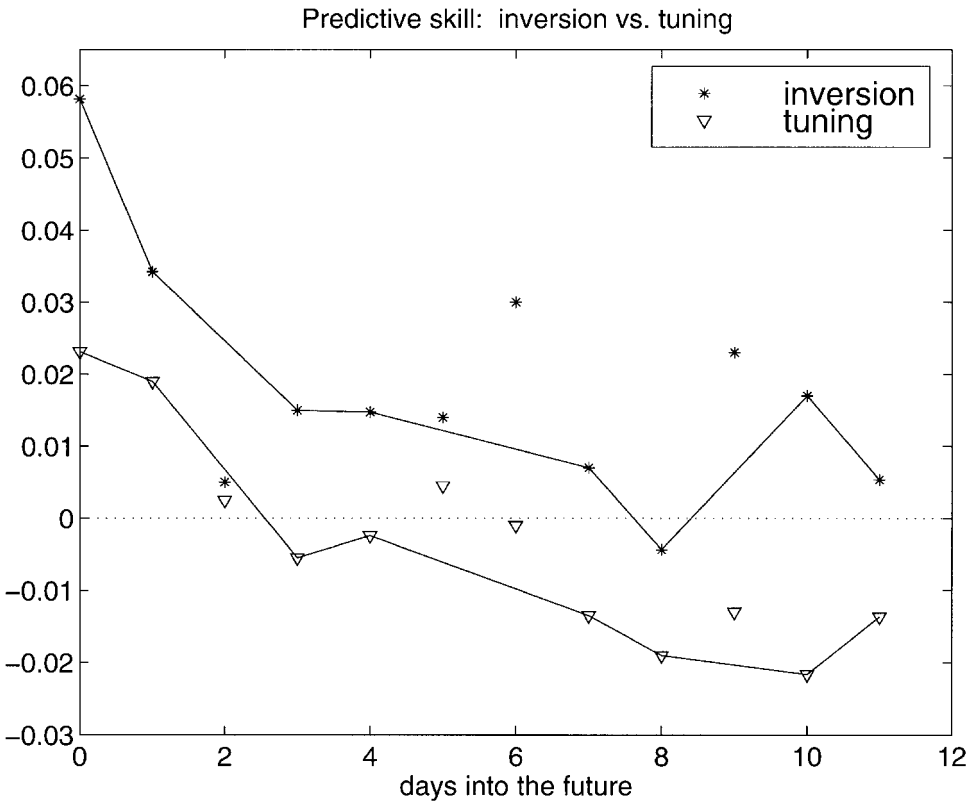

Figure 17. Predictive skill from tuning friction. (The asterisks in Fig. 16 are included here for comparison.) The open circles represent predictive skill obtained by tuning the friction coefficient of the prior model according to ADCP data from a one-day survey, with the same averaging that yielded the asterisks. Note the clear indication of a finite time scale for predictive skill obtained by tuning. Note also that tuning is inferior to inversion, and that tuning actually degrades the prior after one week.

As with any weighted least-squares fit of a linear model, posterior skill for the inverse is guaranteed to equal or exceed prior skill. This is problematic because Davis (1977) shows that sampling errors can degrade forecasts while simultaneously making hindcasts artificially accurate. In particular, Davis shows that errors degrade forecast skill by about the same amount that they increase artificial hindcast skill. The predictability studies in Section 4 check for artificial hindcast skill by comparing inverse adjustments to data other than those used in the inverse. Inversion improves the accuracy of the tidal model, and there is evidence that improvement lasts for only a week. But the inverse rarely degrades the accuracy of the prior. This supports the conclusion that the increase in skill from inversion is real.

Parameter tuning also increases hindcast skill, as it must, but improvements from tuning are not as large as those from inversion. More important, however, is the fact that

parameter tuning actually degrades forecast skill after a week, and forecast degradation is comparable to hindcast improvement. Thus, the model improvements obtained by tuning are consistent with Davis' definition of artificial skill.

A physical explanation for finite time scale of inverse adjustments could lie with any process that affects tidal dynamics on week-long time scales. This could include nonlinear effects associated with the spring-neap cycle (even though prior forcing includes spring-neap variation), wind forcing and/or changes in stratification. For example, Ullman and Wilson (1998) argue that changes in stratification explain the tidal modulation that they observed in ADCP observations from the Hudson River estuary.

Conclusions from the predictability studies are not definitive because the two-week observational program barely resolves the underlying one-week time scale. If confirmed, the predictability results would have important implications for the design of effective sampling strategies. For example, the finite time scale indicates that repeated sampling of the same transect may be superfluous in back to back surveys. Furthermore, spatial inhomogeneities in the posterior error variance indicates that sampling on a uniform grid may be wasteful of ship time. Depending on the scientific objective, the optimal ship track may involve preferential sampling of regions where data effect the largest reduction in posterior error variance. With accurate *a priori* statistics, these issues could be addressed before going out to sea.

Acknowledgments. Financial support from the National Science Foundation through Grant OCE-9633465 made this research possible and is gratefully acknowledged. Also, the Connecticut Department of Environmental Protection supported the data collection through a grant, CWF325-R, from the Long Island Sound Research Fund. The expert skills of the staff at the Marine Sciences and Technology Center at The University of Connecticut made the measurement program smooth, safe, and successful. The staff at N.O.A.A. provided software and tidal constitutents for surface height predictions. The research vessel of choice for this study was provided though a generous donation to The University of Connecticut by Professor Karl Turekian. Comments from Andrew Bennett and an anonymous reviewer helped improve the manuscript. Finally, PSB would like to thank Professor George Veronis for many helpful and stimulating discussions throughout the course of this study.

APPENDIX

The fields of $\hat{\mathbf{u}}$ and $\hat{\eta}$ that minimize (24) are solutions to (7–9) with the optimal dynamical adjustments

$$\hat{\varepsilon}_{u_t}(\mathbf{x}, t) = \int\int \mu_u Q_{u_t} \tag{29}$$

$$\hat{\varepsilon}_{v_t}(\mathbf{x}, t) = \int\int \mu_v Q_{v_t} \tag{30}$$

$$\hat{\varepsilon}_{\eta_t}(\mathbf{x}, t) = \int\int \mu_\eta Q_{\eta_t} \tag{31}$$

$$\hat{\varepsilon}_{obc}(s, t) = \int\int H(\mu_u, \mu_v) \cdot \hat{\mathbf{n}} Q_{obc} \tag{32}$$

where the μ's satisfy

$$\frac{\partial \mu_u}{\partial t} - f\mu_v = -H\frac{\partial \mu_\eta}{\partial x} + \kappa\mu_u - Q_d^{-1}(\mathbf{d} - \mathbf{L}[\hat{\mathbf{u}}]) \cdot \mathbf{L}_u, \tag{33}$$

$$\frac{\partial \mu_v}{\partial t} + f\mu_u = -H\frac{\partial \mu_\eta}{\partial y} + \kappa\mu_v - Q_d^{-1}(\mathbf{d} - \mathbf{L}[\hat{\mathbf{u}}]) \cdot \mathbf{L}_v, \tag{34}$$

$$\frac{\partial \mu_\eta}{\partial t} = -g\left(\frac{\partial \mu_u}{\partial x} + \frac{\partial \mu_v}{\partial y}\right), \tag{35}$$

with coastal boundary condition

$$(\mu_u, \mu_v) \cdot \hat{\mathbf{n}} = 0, \tag{36}$$

open boundary condition

$$(\mu_u, \mu_v) \cdot \hat{\mathbf{n}} = -\sqrt{\frac{H}{g}}\,\mu_\eta, \tag{37}$$

and terminal conditions

$$\mu_\eta(\mathbf{x}, T) = \mu_u(\mathbf{x}, T) = \mu_v(\mathbf{x}, T) = 0. \tag{38}$$

The elements of vectors $\mathbf{L}_u$ and $\mathbf{L}_v$ are numerical representations of delta functions at measurement locations for u and v, respectively. (The numerical delta function has smoothing scales of 1 km and 15 minutes.) The solution is obtained with representers following the procedures described by Bogden *et al.* (1996).

The prior error variance

$$Q_u = \langle (u_{prior}(\mathbf{x}, t) - \langle u(\mathbf{x}, t)\rangle)^2\rangle = \langle (u'(\mathbf{x}, t))^2\rangle \tag{39}$$

is the mean-square error in the prior tidal velocity estimate u_{prior} $(\mathbf{x}, t)$ of east-west tidal velocity u (Fig. 11). This results from propagating the dynamical error covariance through the dynamics. It is obtained by computing the representer associated with a measurement (i.e., evaluation) of $u(\mathbf{x}, t)$ at the location $\mathbf{x}$ and t (Bennett, 1992).

The posterior error variance

$$Q_{\hat{u}} = \langle (\hat{u}(\mathbf{x}, t) - \langle u(\mathbf{x}, t)\rangle)^2\rangle = Q_u - \mathbf{r}^T(\mathbf{R} + Q_d\mathbf{I})^{-1}\mathbf{r}, \tag{40}$$

is the mean-square error in the inverse estimate û of u (Fig. 12). It is obtained with the representer vector $\mathbf{r}(\mathbf{x}, t)$ and the representer matrix $\mathbf{R}$ associated with the data d, as in Bogden *et al.* (1996).

REFERENCES

Bennett, A. F. 1992. Inverse Methods in Physical Oceanography, Cambridge University Press, 346 pp.

Bennett, A. F. and P. C. McIntosh. 1982. Open ocean modeling as an inverse problem: Tidal theory. J. Phys. Oceanogr., *12,* 1004–1018.

Bogden, P. S., P. Malanotte-Rizzoli and R. Signell. 1996. Open-ocean boundary conditions from interior data: Local and remote forcing of Massachusetts Bay. J. Geophys. Res., *101,* 6487–6500.

Bretherton, F. P., R. E. Davis and C. B. Fandry. 1976. A technique for objective analysis and design of oceanographic experiments applied to MODE-73. Deep-Sea Res., *23,* 559–582.

Candela, J., R. C. Beardsley and R. Limeburner. 1990. Removing tides from ship-mounted ADCP data, with application to the Yellow Sea. IEEE Fourth Conference on Current Measurements, 258–266.

—— 1992. Separation of tidal and subtidal currents in ship-mounted acoustic Doppler current profiler observations. J. Geophys. Res., *97,* 769–788.

Davis, R. E. 1977. Techniques for statistical analysis and prediction of geophysical fluid systems. Geophys. Astrophys. Fluid Dyn., *8,* 245–277.

Dowd, M. and K. R. Thompson. 1996. Extraction of tidal streams from a ship-borne acoustic Doppler current profiler using a statistical-dynamical model. J. Geophys. Res., *101,* 8,943–8,956.

Egbert, G. and A. F. Bennett. 1996. Data assimilation methods for ocean tides, *in* Modern Approaches to Data Assimilation in Ocean Modeling, P. Malanotte-Rizzoli, ed., Elsevier Oceanography Series, 61, Elsevier, 147–179.

Foreman, M. G. G. and H. J. Freeland. 1991. A comparison of techniques for tide removal from ship-mounted acoustic Doppler measurements along the southwest coast of Vancouver Island. J. Geophys. Res., *96,* 17,007–17,021.

Geyer, R. and R. Signell. 1990. Tidal flow measurements around a headland with a shipboard acoustic Doppler current profiler. J. Geophys. Res., *95,* 3189–3197.

Gordon, R. L. 1996. Acoustic Doppler Current Profiler: Principles of Operation. RD Instruments, 54 pp.

Joyce, T. M. 1989. On *in situ* calibration of shipboard ADCPs. J. Atmos. Oceanic Tech., *6,* 169–172.

McIntosh, P. C. and A. F. Bennett. 1984. Open ocean modeling as an inverse problem: M_2 tides in Bass Strait. J. Phys. Oceanogr., *14,* 601–614.

Mesinger, F. and A. Arakawa. 1976. Numerical Methods Used in Atmospheric Models, GARP Publication Series No. 14, WMO/ICSU Joint Organizing Committee, 64 pp.

Moody, J. A., B. Butman, R. C. Beardsley, W. S. Brown, P. Daifuku, J. D. Irish, D. A. Mayer, H. O. Mofjeld, B. Petrie, S. Ramp, P. Smith and W. R. Wright. 1984. Atlas of Tidal Elevation and Current Observations on the Northeast American Continental Shelf and Slope. U.S. Geological Survey Bulletin, *1611,* 122 pp.

Münchow, A., R. W. Garvine and T. F. Pfeiffer. 1992. Subtidal currents from a shipboard acoustic Doppler current profiler in tidally dominated waters. Cont. Shelf Res., *12,* 499–515.

Platzman, G. W. 1972. Two dimensional free oscillations in natural basins. J. Phys. Oceanogr., *2,* 117–138.

R. D. Instruments. 1995. Direct reading and self-contained broadband acoustic Doppler current profiler technical manual. R. D. Instruments, San Diego, California.

Simpson, J. H., E. G. Mitchelson-Jacob and A. E. Hill. 1990. Flow structure in a channel from an acoustic Doppler current profiler. Cont. Shelf Res., *10,* 589–603.

Ullman, D. S. and R. E. Wilson. 1998. Model parameter estimation from data assimilation modeling: Temporal and spatial variability of the bottom drag coefficient. J. Geophys. Res., *103,* 5531–5549.

Received: *8 July, 1997;* Revised: *1 June, 1998.*